Effect of Rotations and Shape Resonances on Photoassociation and Photoacceleration by Short Infrared Laser Pulses

P. Backhaus, J. Manz, and B. Schmidt*

Institut für Physikalische und Theoretische Chemie, WE 3, Freie Universität Berlin, Takustrasse 3, D-14195 Berlin, Germany

Received: October 28, 1997; In Final Form: December 2, 1997

A quantum dynamical description of an atomic collision pair interacting with the electric field of a short infrared laser pulse is developed. Inelastic processes in the electronic ground state are due to stimulated emission resulting in photoassociation, or absorption leading to photoacceleration. A perturbative approach based on a state space representation is compared with a numerical treatment using a grid representation in coordinate space. Special emphasis is on the role of rotations and, in particular, of shape resonances. It is shown that these quasibound states which are supported by the centrifugal barrier (for $J \neq 0$) can be used as initial states to effectively populate a selected bound state with specific vibrational and rotational quantum number (photoassociation), or a partial wave of a scattering state with defined energy and rotational quantum number (photoacceleration). Simulations are carried out for the prototype H + Cl collision pair. Also the effect of averaging over initial conditions (velocity, angular momenta) is investigated for a supersonic beam experiment. For a narrow velocity distribution, we predict the presence of a resonance structure of the association and acceleration probability as a function of the mean collision energy.

1. Introduction

When a pair of colliding atoms comes in close contact, the arising dipole moment opens the way for control of the dynamics by electromagnetic fields. The interaction of collision complexes with infrared (IR) radiation can result in two different inelastic scattering events.[1] Stimulated emission of n IR photons may lead to bound ← free transitions, resulting in diatomic molecules in the electronic ground state

$$AB(\epsilon,J) + \hbar\omega \rightarrow AB(v,J) + (n+1)\hbar\omega \qquad (1)$$

where ϵ and J are the scattering energy and the angular momentum associated with the relative motion of the colliding atoms and where v and J are the vibrational and rotational quantum numbers of the photoassociation product. It is suggestive that associative scattering events are most likely when the photon energy $\hbar\omega$ is close to the resonance condition for a transition from the initial scattering state at energy ϵ to any of the bound states levels $E(v,J)$ of the molecule AB

$$E(\epsilon,J) - E(v,J) \approx n\hbar\omega \qquad (2)$$

This photoassociative event competes with free ← free transitions of the collision pair

$$AB(\epsilon,J) + n\hbar\omega \rightarrow AB(\epsilon',J) \qquad (3)$$

where absorption of n photons results in photoacceleration of the colliding particles with

$$E(\epsilon',J) - E(\epsilon,J) \approx n\hbar\omega \qquad (4)$$

This type of inelastic scattering event is also known in the literature as collision induced absorption.[2] It is noted that a third class of light-induced scattering event is the absorption of photons leading to molecular products in an electronically excited state. This type of photoassociation is not considered in the present work, because this pathway is not usually accessible by IR radiation. However, it is the dominant mechanism for visible (vis) and ultraviolet (UV) photoassociation which has been studied extensively for systems such as alkali metals,[3−9] rare gas halides,[10,11] and certain metals in the second column of the periodic table,[12] in particular mercury.[13−15]

The application of pulsed subpicosecond IR lasers to induce photoassociation according to eq 1 has been proposed recently for the first time[16] in analogy to previous work on the reversed process of photodissociation using pulsed IR lasers.[17,18] In simulations for the collision pair O + H it has been shown that, by optimal design of laser pulses, photoassociation can be made very efficient for near-resonant cases and that a very high selectivity with respect to the vibrational state of the OH molecule can be achieved.[16] In a subsequent study also the control of photoacceleration according to eq 3 for nonresonant cases has been investigated.[19] It has been shown that there are distinct maxima in the distribution of the energy ϵ' of the scattered particles, which can be attributed to the absorption of one or more IR-photons. The possibility of IR ps laser pulse induced transitions between resonances embedded in the continuum has already been investigated in ref 20; in particular it was shown that transitions from long-lived to short-lived resonance may be used to control the dissociative decay rate of triatomic model systems.

In the present work, we extend the previous studies by including the effect of rotations which had been neglected in the one-dimensional rotationless models of refs 16, 19, 20. The inclusion of rotational effects should open new spectroscopic transition pathways in the manifold of ro-vibrational states of the association product AB similar to the case of IR photodissociation.[18] In particular we shall investigate the possibility of using photoassociation to prepare molecules in a specific ro-vibrational quantum state, or photoacceleration to prepare

S1089-5639(98)00005-X CCC: $15.00
Published on Web 02/12/1998

collision pairs at a certain energy and in a specific angular momentum eigenstate (partial wave). Some problems that will have to be addressed include the efficiency of laser induced association versus acceleration, and also the selectivity with respect to the quantum state of the product.

Our main focus is on new effects that can be expected for collisions with $J \neq 0$ where a centrifugal barrier separates the attractive potential well from the asymptotic region, giving rise to shape resonances for collision energies ϵ lower than the barrier height.[21,22] Observations of these resonances in atomic beam scattering experiments have been reported in ref 23. The wave functions corresponding to these quasi-bound states exhibit a high probability amplitude in the region of the well of the effective potential where the dipole moment is strongest. Thus, we expect that resonance states can be manipulated far more effectively by external fields than nonresonant scattering states if their lifetime is long compared to the laser pulses used to induce an inelastic scattering event. It is noted that, due to their large geometric cross sections and their relatively long lifetimes, shape resonances also play an important role in the process of (termolecular) collision induced association reactions (recombination).[24−27] In summary, the manipulation of shape resonance states of collision pairs opens the way not only to a new kind of spectroscopy of quasi-bound states trapped behind a centrifugal barrier[9] but also, as we shall demonstrate below, to a novel approach to IR-sub-picosecond laser control of photoassociation versus acceleration.

The possibility of observing the effect of shape resonances experimentally crucially depends on the preparation of the collision pairs, because the width of the shape resonances is extremely narrow and their spacing is not very wide compared to thermal energy distributions. Indeed, the first direct experimental observation of individual shape resonances has been demonstrated only recently in a study on ultracold collisions of Rb atoms.[9] At thermal energies, however, superpositions of a large number of partial waves with different angular momentum J and averaging over a distribution of collision energies ϵ has to be taken into account so that the effect of shape resonances on the photoassociation probability may be obscured. Instead, we propose an experiment using supersonic nozzle beams yielding relatively narrow velocity distributions.[28] Simulations of laser induced control of collision pairs will be carried out, and the question will be discussed whether the resonance structure can be observed in beam experiments with varying energy resolution. As a model, diatomic hydrides should be especially suitable, due to the relatively large spacing of vibrational and rotational energy levels. In particular, we choose H + Cl collisions in the present study.

The organization of the article is as follows: Our model, as well as the various levels of approximation used in the quantum dynamical simulations, is developed in section 2. In the following section 3 we present and discuss our results. The final section 4 gives our conclusions.

2. Methods

2.1. Model. The quantum dynamics of photoinduced inelastic scattering of the H + Cl collision pair is governed by the Hamilton operator

$$\hat{H}(t) = \hat{H}_{\mathrm{mol}} + \hat{W}(t) \tag{5}$$

where the time-independent molecular Hamiltonian can be expressed in spherical components r, θ_r, ϕ_r of the internuclear distance vector $\vec{r}$

$$\hat{H}_{\mathrm{mol}}(\vec{r}) = -\frac{\hbar^2}{2m}\frac{\partial^2}{\partial r^2} + \frac{\hat{J}^2(\theta_r,\phi_r)}{2mr^2} + V(r) \tag{6}$$

where $m = 0.97u$ is the reduced mass and $\hat{J}$ is the angular momentum of the $^1H + {}^{35}Cl$ system. In the framework of the Born−Oppenheimer approximation, only the potential energy curve for the electronic ground state is considered, which is modelled by a Morse potential function

$$V(r) = D_e\{1 - \exp[-\beta(r - r_e)]\}^2 - D_e \tag{7}$$

with experimentally determined values of $r_e = 0.1275$ nm for the equilibrium bond length, $D_e = 37249.2$ cm^{-1} for the dissociation energy, and $\beta = 0.01868$ nm^{-1} for the steepness parameter.[29]

The time-dependent part of the Hamiltonian describes the interaction between the molecular dipole moment $\vec{\mu}$ and an external electric field $\vec{\epsilon}(t)$ in the semiclassical dipole approximation[30]

$$\hat{W}(t) = -\vec{\mu}(r)\vec{\epsilon}(t) = -\hat{\mu}(r)\epsilon(t)\cos(\theta_r) \tag{8}$$

Here it is assumed that $\vec{\epsilon}$ is polarized along the z-axis, and θ_r is the angle between $\vec{\mu}$ and $\vec{\epsilon}$. We adapt a dipole moment function for HCl from the literature[31] using a spline fit to interpolate between the tabulated values. The electric field of the laser pulse is of the form

$$\vec{\epsilon}(t) = \vec{\epsilon}_p g_p(t)\cos(\omega_p t) \tag{9}$$

where $|\vec{\epsilon}_p|$ and ω_p are the amplitude and the frequency of the pulse, respectively. A convenient choice of the pulse shape is given by the function

$$g_p(t) = \sin^2\left(\frac{\pi t}{2T_p}\right), \quad 0 \le t \le 2\,T_p \tag{10}$$

with a pulse duration $2\,T_p$, which is very similar to a Gaussian pulse shape with a fwhm of T_p but offers the advantage of a well-defined beginning and end of the pulse.

2.2. Bound and Continuum States. Throughout most of this paper, representations in a basis of bound and free eigenstates will be used. The corresponding wave functions in position space are obtained by solving the one-dimensional time-independent Schrödinger equation

$$\left[-\frac{\hbar^2}{2m}\frac{\partial^2}{\partial r^2} + V_{\mathrm{eff},J}(r)\right]\chi_{vJ}(r) = E_{v,J}\chi_{v,J}(r) \tag{11}$$

for an effective potential including a term for the centrifugal barrier

$$V_{\mathrm{eff},J}(r) = V(r) + \frac{J(J+1)\hbar^2}{2mr^2} \tag{12}$$

Bound state wave functions can be written as a product of a radial and a spherical harmonic function

$$\langle \vec{r}\,|vJM\rangle = \frac{\chi_{v,J}(r)}{r}Y_{J,M}(\theta_r,\phi_r) \tag{13}$$

To solve eq 11 numerically, we calculate the discrete eigenvalues and the corresponding radial eigenfunctions using a Fourier-grid Hamiltonian method.[32] The Morse potential of eq 7 with the parameters for electronic ground state of HCl supports

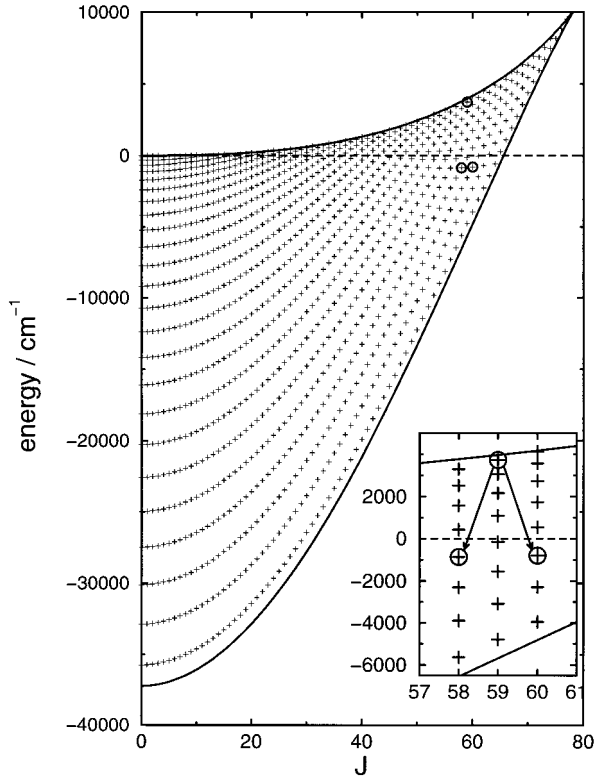

Figure 1. Bound states and resonance states for the electronic ground state of HCl. The envelopes illustrate the *J*-dependence of the well depth and of the barrier height of the effective potential energy curve (eq 12). The insert shows the two possible transitions from the ($v = 7$, $J = 59$) resonance state to the (3,58) or (2,60) bound states induced by laser pulses as specified in the text.

a total number of 984 bound states for $0 \le J \le 65$ where the number of bound states varies from 24 for $J = 0$ to a single state for $J = 65$. The resulting bound levels are shown in Figure 1. For comparison, the minima (wells) and maxima (centrifugal barriers) of the effective potential energy curves with respect to *J* are also shown as interpolated solid curves.

Free states can be represented in position space by a basis set similar to expression 13

$$\langle \vec{r} \,|kJM\rangle = \frac{4\pi}{(2\pi)^{3/2}} \frac{1}{k} \frac{\chi_{k,J}(r)}{r} Y_{J,M}(\theta_r,\phi_r) \qquad (14)$$

Here the continuous radial wave function $\chi_{k,J}(r)$ is normalized asymtotically with respect to $\sin(kr - J\pi/2 + \delta_J)$ with a phase shift δ_J.

In our calculations we use scattering states which are linear combinations of eqs 14

$$\langle \vec{r} \,|\vec{k}\rangle = \frac{4\pi}{(2\pi)^{3/2}} \frac{1}{k} \sum_J \sum_M i^J e^{i\delta_J} \frac{\chi_{k,J}(r)}{r} Y^*_{J,M}(\theta_k,\phi_k) Y_{J,M}(\theta_r,\phi_r) \quad (15)$$

These scattering states exhibit the asymptotic behavior of an incoming plane wave with a specific momentum $\hbar\vec{k}$ and of outgoing spherical waves. The scattering energy of this state is ϵ with $k = 1/\hbar\sqrt{2m\epsilon}$. We emphasize, that we do not use localized wave packets as initial states, but stationary scattering functions of the form of eq 15 because we do not want the final results to depend on the actual choice of the inital wave packet. Our approach is also much more general since it is possible to construct any wave packet from a linear combination of stationary scattering states.

The corresponding radial wave functions $\chi_{k,J}(r)$ are calculated by numerical integration of the radial Schrödinger eq 11 with $\epsilon > 0$ starting from the classically forbidden region ($r \to 0$) by a Bulirsch−Stoer method.[33] The solutions are truncated in the asymptotic region at ca. 5.2 nm and fitted to $\sin(kr - J\pi/2 + \delta_J)$.

2.3. Inelastic Scattering Cross Sections. In the following we want to define inelastic scattering cross sections for the processes of photoassociation and photoacceleration using pulsed light sources. We proceed in close analogy to elastic scattering theory where the collision pair asymptotically approaches the superposition of an incoming plane wave characterized by its momentum $\hbar\vec{k}$ and outgoing spherical waves and where the elastic differential scattering cross section $d\sigma/d\Omega$ is given as

$$\frac{d\sigma}{d\Omega} = \frac{J_o r^2}{|J_i|} \qquad (16)$$

where J_i is the incoming and J_o is the outgoing probability current scattered into $d\Omega$ which for sufficiently large r is inversely proportional to r^2.[34]

In our quantum-mechanical description, we are dealing with probability amplitudes $|c(t)|^2$ obtained from quantum-mechanical states which can be expressed as

$$|\Psi(t)\rangle = \sum\!\!\int_n c_n(t) e^{iE_n t/\hbar} |n\rangle \qquad (17)$$

where $|n\rangle$ represent either bound $|vJM\rangle$ (eq 13) or free $|kJM\rangle$ (eq 14) eigenstates of the unperturbed system given by eq 6. Note that here and in the following, the combined sum/integral denotes a sum over all discrete (bound) states and an integration over the continuum (free) states, so that $|c_{vJM}(t)|^2$ is a (dimensionless) probability and $|c_{kJM}(t)|^2$ has the dimension of a probability per volume in momentum space.

For collision pairs interacting with time-dependent external fields, eq 16 must be replaced by an equation for the quantum mechanical probability of finding the collision partners initially prepared in a scattering state *i* of the form of eq 15 in a final state *f*. This probability per unit time and per volume in momentum space is the product of the incoming probability current $J_i = \hbar k/\mu$ and a time-dependent partial inelastic cross section for the transition $f \leftarrow i$ (for $f \neq i$). Therefore we can define $d\sigma_{fi}(t)/d\Omega$ (with the dimension of an area),

$$\frac{d\sigma f_i(t)}{d\Omega} := \frac{1}{|J_i|} \frac{d}{dt} |c_f(t)|^2 \qquad (18)$$

which is differential with respect to the direction of the incoming wave defined by θ_k, ϕ_k in eq 15. Note that the *z*-axis is already given by the direction of the laser polarization. If *f* is a continuum state, this equation gives the probability of finding the system in a state between *f* and $f + df$ and $d\sigma/d\Omega$ will have to be replaced by a doubly differential cross section $d^2\sigma/(d\Omega df)$. Integration over the duration of the light pulse (eq 10) then yields time averaged partial cross sections

$$\frac{d\sigma_{fi}^{p}}{d\Omega} = \frac{1}{2T_p} \int_0^{2T_p} \frac{d\sigma_{fi}(t)}{d\Omega} dt = \frac{|c_f(t = 2T_p)|^2}{2T_p |J_i|} \qquad (19)$$

Summation over all final states gives the total cross section for inelastic scattering for a given initial state *i*. We also define the association cross section $d\sigma_i^{ass}/d\Omega$ as the summation over all final bound states $f = |vJM\rangle$ and the acceleration cross section σ_i^{acc} as the integration over all final free states $f = |kJM\rangle$.

$$\frac{d\sigma_i^{ass}}{d\Omega} = \sum_{vJM} \frac{d\sigma_{fi}^{p}}{d\Omega}; \quad \frac{d\sigma_i^{acc}}{d\Omega} = \sum_{JM} \int_k dk\, k^2 \frac{d\sigma_{fi}^{p}}{d\Omega} \tag{20}$$

We note that the actual value of the association and acceleration cross section will depend on the laser parameters. In particular, the actual size of the cross sections can be easily controlled by changing the amplitude of the laser pulse. The time-dependent coefficients $|c_f(t)|^2$ and hence the inelastic cross sections $d\sigma_{fi}^{p}/d\Omega$ are obtained by numerical integration of the time-dependent Schrödinger equation. In the following subsections we will present two different numerical techniques used in the present investigation.

2.4. Numerical Solution. In our nonperturbative approach we solve the time-dependent Schrödinger equation in position space. In spherical coordinates the initial wave function $\psi_i(\vec{r};t)$ can be expressed generally in terms of spherical harmonics Y_{JM}

$$\langle \vec{r}\,|\psi(t)\rangle = \sum_{JM} \frac{\phi_J(r;t)}{r} Y_{JM}(\theta_r,\phi_r) \tag{21}$$

Note that a negative imaginary potential is used to avoid the effect of the periodic boundary conditions.[35] Inserting this approach into the time-dependent Schrödinger equation and projection on $|Y_{JM}\rangle$ results in a set of coupled partial equations for the time-dependent radial wave functions

$$i\hbar \frac{\partial}{\partial t}\phi_J(r;t) = \left[-\frac{\hbar^2}{2m}\frac{\partial^2}{\partial r^2} + V_{\mathrm{eff},J}(r)\right]\phi_J(r;t) - \mu(r)\epsilon(t)\sum_{J'M'} S_{JMJ'M'}\phi_{iJ'}(r;t) \tag{22}$$

with the Hönl−London factors[36]

$$S_{JM,J'M'} := \int_0^{\pi} d\theta_r \sin\theta_r, \int_0^{2\pi} d\phi_r Y^*_{J,M}(\theta_r,\phi_r)\cos(\theta_r) Y_{J',M'}(\theta_r,\phi_r)$$
$$= \sqrt{\frac{(J-M)(J+M)}{(2J-1)(2J+1)}}\delta_{J,J'+1}\delta_{M,M'} + \sqrt{\frac{(J-M+1)(J+M+1)}{(2J+1)(2J+3)}}\delta_{J,J'-1}\delta_{M,M'} \tag{23}$$

representing the matrix elements of the direction cosine $\cos\theta_r$ (eq 8) in the basis of spherical harmonics.

The radial wave functions are represented on an equally spaced grid which facilitates evaluation of the kinetic energy operator T by FFT techniques.[37] The grid consists of 4096 points covering the range up to $r = 5.3$ nm where we had to cut off the scattering wave function. The relatively large grid size was chosen to avoid effects of the finite grid size on the photoinduced dynamics. Though we considered J-values from 0 to 77 in our calculations, we never propagated more than three neighboring J-terms at the same time. That means we just coupled three different partial waves together and not the whole range of 78 partial waves. For weak couplings which means weak laser fields this will be a good approximation.

For sufficiently small time steps Δt, the Hamiltonian of eq 5 can be regarded to be time-independent thus permitting an easy evaluation of the time evolution operator using the split operator[38,39]

$$\psi(t+\Delta t) = e^{-i\Delta t/\hbar \hat{H}}\psi(t) = e^{-i\Delta t/2\hbar}e^{-i\Delta t\hat{V}/\hbar}e^{-i\Delta t\hat{T}/2\hbar}\psi(t) + O(\Delta t)^3 \tag{24}$$

Typically, a time step of 0.1 fs was used to propagate from $t = 0$ to $t = 2T_p$. Finally, the coefficients $|c_f(t = 2T_p)|$ in eq 17 are obtained by projecting the time-dependent wave functions $\langle \vec{r}|\psi_i(t)\rangle$ on that of the final states f as given by eqs 13 and 14.

2.5. Perturbation Theory. In our perturbative approach we use a state space representation. Inserting the *ansatz* of eq 17 into the time-dependent Schrödinger equation and projecting on one of the eigenstates yields a system of coupled first order integro-differential equations for the time-dependent expansion coefficients $c_n(t)$

$$i\hbar \frac{d}{dt}c_n(t) = \sum_m \int W_{nm}(t) e^{i\omega_{nm}t} c_m(t) \tag{25}$$

Here $W_{nm}(t) = \langle n|W(t)|m\rangle$ gives the matrix elements of the perturbation operator for the $n \leftarrow m$ transition, and $\omega_{nm} = (E_n - E_m)/\hbar$ is the corresponding Bohr frequency.

The usual approach of time-dependent perturbation theory for weak interaction assumes negligible changes of the population numbers, thus rendering the coefficients $c_m(t) = c_m(t = 0)$ on the right hand side of eq 25 to be independent of time.[4] Hence, for the system initially prepared in state i, we obtain for the coefficient of the final state $f \neq i$

$$\frac{d}{dt}c_f(t) = -\frac{1}{2i\hbar}\langle f|\hat{\vec{\mu}}\cdot\vec{\epsilon}_p|i\rangle \sin^2\left(\frac{\pi t}{2T_p}\right)(e^{i\Omega_{fi}^{+}t} + e^{i\Omega_{fi}^{-}t}) \tag{26}$$

where the expression 8 for the electric dipole interaction operator and the explicit time−dependence (eq 9) of the electric field has already been inserted and where the detuning of the light frequency from the Bohr frequency is given by

$$\Omega_{fi}^{\pm} := \pm\omega_p + \frac{E_f - E_i}{\hbar} \tag{27}$$

Integration of eq 26 over the perturbation time (pulse duration) then yields the coefficients at the end of the laser pulse

$$c_f(2T_p) = \frac{T_p}{2\hbar}\langle f|\vec{\mu}\cdot\vec{\epsilon}_p|i\rangle (G(\Omega_{fi}^{+}T_p) + G(\Omega_{fi}^{-}T_p)) \tag{28}$$

where the effective line shape function G is obtained as the Fourier transform of the $\sin^2$-like pulse shape function

$$G(\Omega_{fi}^{\pm}T_p) := \frac{1}{iT_p}\int_0^{2T_p} dt \sin^2\left(\frac{\pi t}{2T_p}\right)e^{\Omega_{fi}^{\pm}t} = \frac{e^{i2\Omega_{fi}^{\pm}T_p} - 1}{2\Omega_{fi}^{\pm}T_p[(\Omega_{fi}^{\pm}T_p/\pi)^2 - 1]} \tag{29}$$

Assuming the light pulse being long compared to the Bohr period ($2T_p \gg 1/\omega_{fi}$), either $G(\Omega_{fi}^{-}T_p)$ or $G(\Omega_{fi}^{+}T_p)$ will be neglected for stimulated emission ($E_f < E_i$) or absorption ($E_f > E_i$), respectively (resonant approximation).

For the photoinduced processes under investigation, analytical expressions for the coefficients c_f of eq 28 can be given with the help of the position space representations of bound eq 13 and free eq 14 states. First, we define the radial matrix element of the dipole moment function

$$\mu_{fi} := \int_0^{\infty} dr\, \chi_f^*(r)\mu(r)\chi_i(r) \tag{30}$$

where i and f represents either v, J for bound states or k, J for scattering states. These matrix elements are obtained numerically from the grid representations of the radial wavefunctions $\chi(r)$ (see previous section). Their squares give the Franck−Condon factors of the corresponding transition. For a discussion of the peculiarities of these factors for bound ← free transitions, we refer to the review in ref 40.

For the photoassociation transition from an initial scattering state $|\vec{k}_i\rangle$ to a bound state $|vJM\rangle$ (eq 13) the coefficients of the bound states at the end of the laser pulse are

$$c_{vJM}(2T_p) = -\frac{4\pi}{(2\pi)^{3/2}}\frac{\epsilon_p T_p}{2\hbar}\frac{1}{k_i}\sum_{J'M'}\{i^{J'}e^{i\delta_{J'}}Y^*_{J',M'}(\theta_{k_i},\phi_{k_i}) \times S_{JM,J'M'}\mu_{vJ,k_iJ'}G(\Omega^+_{vJ,k_iJ'}T_p)\} \quad (31)$$

Accordingly, the transition from the same initial scattering state $|\vec{k}_i\rangle$ to a specific partial wave $|kJM\rangle$ (eq 14) of the photoaccelerated collision pair can be described by the coefficients

$$c_{kJM}(2T_p) = -\frac{(4\pi)^2}{(2\pi)^3}\frac{\epsilon_p T_p}{2\hbar}\frac{1}{kk_iJ'M'}\sum\{i^{J'}e^{i\delta_{J'}}Y^*_{J',M'}(\theta_{k_i},\phi_{k_i}) \times S_{JM,J'M'}\mu_{kJ,k_iJ'}G(\Omega^-_{kJ,k}i_{J'}T_p)\} \quad (32)$$

In the present work, a further simplification of eqs 31 and 32 is reached by assuming the incoming plane waves $\vec{k}_i$ to be parallel to the z-axis (and hence to the polarization direction of the electric field). Then the expression for the spherical harmonics[36]

$$Y_{J,M}(\theta_{k_i}=0,\phi_{k_i}) = \sqrt{\frac{2J+1}{4\pi}}\delta_{M,0} \quad (33)$$

eliminates the summation over M' in eqs 31 and 32, so that the problem is reduced to a two-dimensional one $M' = 0$. Apart from being computationally much easier to solve, the perturbation ansatz also offers a much easier interpretation of the inelastic cross sections. From the above equations it is clear that, apart from normalization factors, the cross sections are proportional to Franck−Condon and Hönl−London factors as well as the effective line shape function (eq 29) of the pulsed light source. However, there may be interferences between the two terms corresponding to the only nonvanishing Hönl−London factors (see eq 23) for $J' = J + 1$ and $J' = J - 1$. In the present investigation these interference effects do not play a major role, because, for a given scattering energy coinciding with a shape resonance, the Franck−Condon factors are only large for one specific value of J'.

3. Results

3.1. Shape Resonances. Shape resonances are located in two different ways. First, scattering states are calculated by integrating the Schrödinger equation numerically as described above and monitoring the phase shift $\delta_J(\epsilon)$ as a function of the scattering energy ϵ. Normally, this function changes slowly with respect to the scattering energy ϵ except at the resonance energies ϵ_R where it changes rapidly by π (for an example, see Figure 2) which allows us to determine the position and width of quasibound shape resonances. The latter is obtained from

$$\Gamma = 2\left(\left.\frac{d\delta_J}{d\epsilon}\right|_{\epsilon=\epsilon_R}\right)^{-1} \quad (34)$$

For comparison, we use the program LEVEL 6.0 by R. J. LeRoy[41] which employs an Airy function boundary condition method to determine the resonance energies, as well as a uniform semiclassical approximation to calculate their widths. The results obtained from these two approaches are found to be in good agreement with each other. For $9 \le J \le 77$ we discover a total of 176 quasibound states which are also included in Figure 1. Although resonance states are not truly bound states, we designate quasibound states according to the number v of nodes within the potential well formed by the centrigugal barrier.

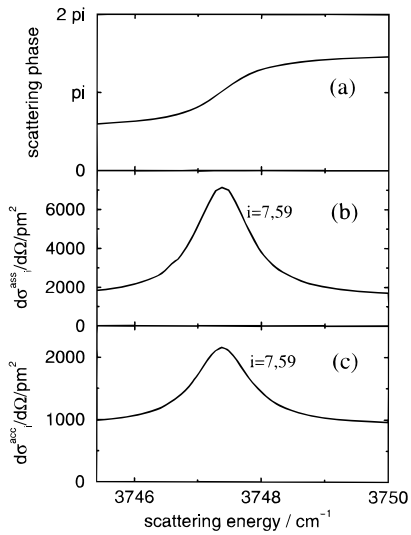

Figure 2. (a) Scattering phase $\delta_{59}(k)$ in the vicinity of the ($v = 7$, $J = 59$) resonance state at $\epsilon_0 = 3747.4$ cm^{-1}. The maximum slope is used to determine position and width of the resonance state (see eq 34). (b) Association cross section versus scattering energy ϵ. The peak is mainly due to the (3,58) ← (7,59) transition. (c) Acceleration cross section vs scattering energy.

The calculated lifetimes $\tau_R = \hbar/\Gamma$ of the resonance states vary greatly with the vibrational quantum number where the highest quasibound states just below the centrifugal barrier exhibit shortest lifetimes. For our model of the HCl molecule, the shortest-lived resonance state is found for ($v = 10$, $J = 53$) with $\tau_R = 150$ fs, $\Gamma = 35$ cm^{-1}. However, this is a rather untypical case because it almost coincides with the height of the centrifugal barrier. Most resonances exhibit lifetimes of at least a picosecond or, in many cases, considerably longer. This corresponds to energetic widths of $\Gamma \le 1$ cm^{-1}.

In the following, we focus our attention on the energetically most isolated quasibound state as the best candidate for state-selective processes. Surveying the resonance energies, one finds that this is the (7,59) state at $\epsilon_0 = 3747.4$ cm^{-1} which is separated by more than 120 cm^{-1} from its lower and upper neighbors (4,63) and (5,62).The energetic width of the (7,59) state $\Gamma = 1.0352$ cm^{-1} corresponds to a lifetime of $\tau_R = 5.13$ ps. The wavefunction and the effective potential (eq 12) for $J = 59$ is illustrated in Figure 3. Although most of the probability amplitude $|\psi(r)|^2$ is inside the potential well, there is yet some amplitude outside in the asymptotic region, which is typical for the very highest quasibound states because of the nonnegligible effect of tunneling.

3.2. Population Dynamics. In this section we study the process of laser-induced stabilization of the (7,59) resonance state at $\epsilon_0 = 3747.4$ cm^{-1} by transition to the highest bound state (at negative energy). With the selection rule $\Delta J = \pm 1$ being valid, these are the (3,58) state at $\epsilon = -852.4$ cm^{-1} and the (2,60) state at $\epsilon = -794.1$ cm^{-1} (see the insert of Figure 1). To get the population dynamics of the association process, we use our nonperturbative treatment. For simplicity, we choose

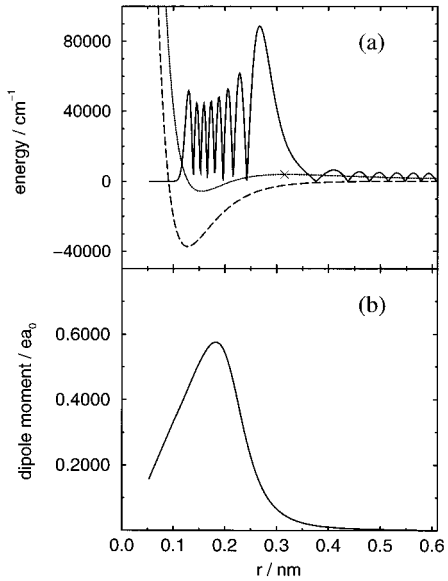

Figure 3. (a) Effective potential energy curves for $J = 0$ (dashed) and $J = 59$ (dotted) and quasibound wave function (solid) for the (7, 59) shape resonance at $\epsilon = 3747.4$ cm^{-1}. The cross indicates the position of the maximum (centrifugal barrier) of the effective potential. (b) Dipole moment function for the electronic ground state of HCl, adapted from ref 31.

the initial wave function (eq 21) to be a single partial wave of the scattering state (eq 15)

$$\phi_{k_0,J}(r, t = 0) = \delta_{59,J}\delta_{0,M}\left\{\frac{1}{(2\pi)^{3/2}k_0} i^J e^{i\delta_J} \sqrt{4\pi(2J+1)}\chi_{k_0 J}(r)\right\} \quad (35)$$

with $k_0 = 1/\hbar\sqrt{2m\epsilon_0}$. Then we solve the coupled partial differential eqs 22 for $J \in [58; 60]$ and $t \in [0; 2T_p]$. By projection on the bound states (eq 13) we calculate the squares of the expansion coefficients $|c_{vJ}(t)|^2$ for values of $J = 58,60$ and $v = (0, 1, 2, 3)$. We optimize the laser pulse in such a way, that the population transfer to the (3,58) state will be maximized. For constant amplitude of the field $\epsilon_p = 514$ MV/m corresponding to a maximum pulse intensity of $I_p = 3.5 \times 10^{10}$ W/cm^2 and for constant pulse duration $2T_p = 200$ fs, we obtain the optimal frequency of $\omega_p = 4605.9$ cm^{-1} which implies a detuning of $\Omega^+ = -6.6$ cm^{-1} with respect to the Bohr frequency of the (3,58) ← (7,59) transition. The resulting population dynamics is shown in Figure 4. During the pulse duration of 200 fs, we see a continuous rise of the target state population (3,58). Although the (2,60) state is energetically very close to the (3,58), the population of the latter remains by approximately 3 orders of magnitude lower than that of the former. Furthermore, we see an intermediate buildup of population in the other vibrational states of the $J = 58$ manifold. As has been shown in our previous study on photoassociation and photoacceleration,[19] the contribution of these states is relatively small unless the frequency is near-resonant for higher order processes. For the given example with the frequency ω_p being about halfway between the resonance condition for two-photon transitions to either the (0,58) or the (1,58) level, the corresponding populations are found to be several orders of magnitude below that of the (3,58) state. We also tried to optimize the laser pulse with respect to population of the (2,60) target level. The resulting population of the target state is about one order of magnitude smaller than for the previous case, because the Franck−Condon factor (see eq 30) sensitively depends on the difference in the vibrational quantum numbers of initial and final state.

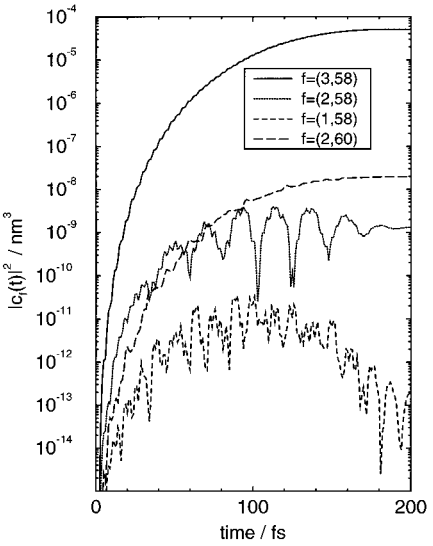

Figure 4. Population dynamics for the photoassociation $f = (v, J) \leftarrow i = (7, 59)$ for the optimized laser pulse (see text). The duration of the laser pulse is 200 fs ($T_p = 100$ fs).

3.3. Validity of Perturbative Treatment. We now compare the numerical and perturbative treatment for the example of the transition from the (7,59) shape resonance to the (3,58) bound state, which was already investigated in the previous section. The comparison is performed by calculating the partial cross section $d\sigma^p_{3,58;7,59}/d\Omega$ which is obtained by averaging over the duration of the laser pulse according to eq 19. The amplitude ϵ_p of the electric field, and hence the intensity of the pulse, is varied, while the values of all other pulse parameters are those of the optimized pulse.

The numerical treatment follows the description in section 3.2, and the cross section is calculated for different values of the laser amplitude $\epsilon_p \in [514$ MV/m; 262 GV/m]. This corresponds to an intensity between 3.5×10^{10} and 9.1×10^{14} W/cm^{-2}. In the perturbative treatment we use eq 31 to calculate $|c_{3,58}(2T_p)|^2$ and hence $\sigma^p_{3,58;7,59}$. In both cases, we simplify the simulations by assuming the incoming plane wave to be parallel to the electric field (see eq 33), and by assuming the initial state to comprise of a single partial wave (see eq 35). The comparison of the results obtained for the two approaches is shown in Figure 5.

It is clear that for the first-order perturbative treatment the partial cross section varies linearly with respect to the pulse intensity, because the coefficient $c_{3,58}(2T_p)$ in eq 31 depends linearly on ϵ_p. The two methods are in very good agreement for laser intensities up to 5×10^{12} W/cm^{-2}. Up to this point the linear rise of the perturbation-based result exactly matches the numerically values for partial cross section as can be seen in Figure 5. Beyond that threshold, the numerical values start to level off and the discrepancy between the two sets of results increases rapidly with the intensity. Our perturbative treatment is not suitable to describe the nonlinear effects occuring in this regime unless higher order terms are included, which, however, would lead to considerably more complicated expressions for the cross sections. All calculations in the remainder of the present work, with the exception of this comparison, were carried out for an electric field amplitude of $\epsilon_p = 514$ MV/m (corresonding to 3.5×10^{10} W/cm^2). Hence, all the cross sections displayed in Figures 6−10 can be enlarged by two orders of magnitude with the perturbation ansatz still being valid. It is noted that, for intensities of about 10^{13} W/cm^{-2}, the

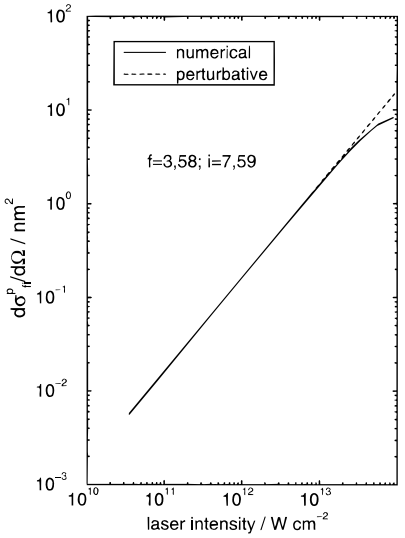

Figure 5. Partial cross section for the association (3, 58) ← (7, 59) vs laser intensity. The remaining parameters are those of the optimized pulse ($2T_p$ = 200 fs, ω_p = 4605.9 cm^{-1}). Comparison of numerical (solid curve) and perturbative treatment (dashed curve).

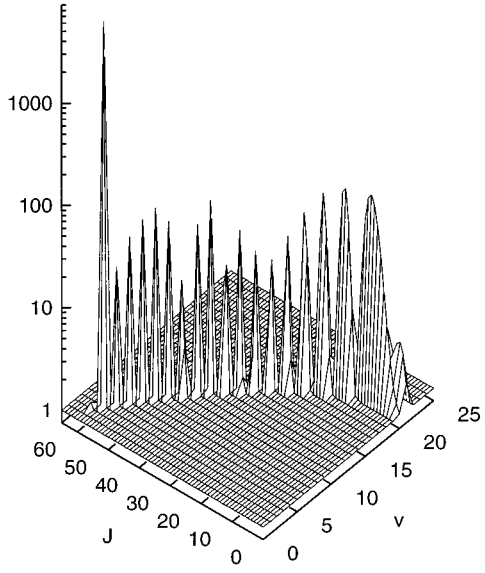

Figure 6. Partial cross section $d\sigma^{P}_{fi}/d\Omega$ (in pm^2, with an offset of 1 pm^2) for the association process with i = (7, 59) and f = (v, J) using the optimized laser pulse (ϵ_p = 514 MV/m, $2T_p$ = 200 fs, ω_p = 4605.9 cm^{-1}).

photoassociation cross sections can be quite large approaching values of a few nm^2.

3.4. State Selectivity. After the investigation of the population dynamics in section 3.2, where the initial state was assumed to be a *single* partial wave (eq 35), we now want to discuss the question of state selectivity of the photoassociation product for the initial state being a full scattering state as given by eq 15 comprising of *all* partial waves. We again consider a scattering energy of ϵ_0 = 3747.4 cm^{-1} exactly coinciding with the (7,59) shape resonance and the laser pulse optimized for the (3,58) ← (7,59) transition.

As anticipated in the introduction, the non-resonant partial waves ($J \neq 7$) exhibit much lower probability amplitude than the resonant partial wave in the region of short internuclear separations where the dipole moment function is nonvanishing. Hence, their individual contribution to the photoassociation probability is much smaller. The photoassociation cross sections as a function of the quantum numbers (v, J) of the final bound

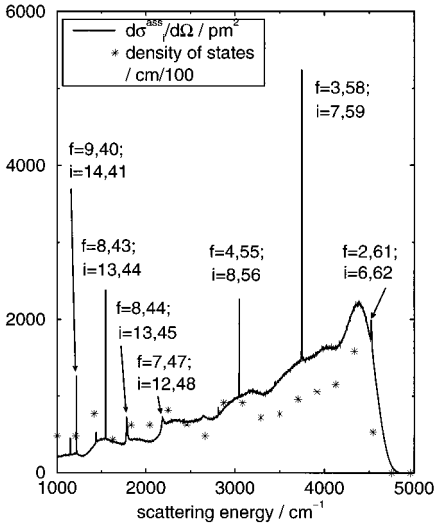

Figure 7. Association cross section $d\sigma_i^{ass}/d\Omega$ as a function of different initial scattering energies (solid line). Some of the peaks in the spectrum are labeled with quantum numbers according to the main bound ← resonance transition. The stars show the density of bound states per energy interval of 0.01 cm^{-1} shifted by the laser energy 4606 cm^{-1}.

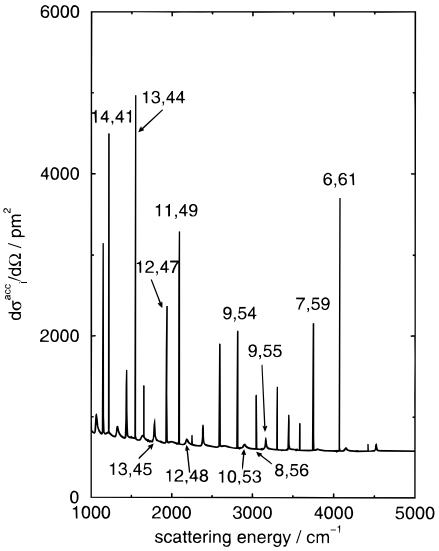

Figure 8. Acceleration cross section $d\sigma_i^{acc}/d\Omega$ as a function of different initial scattering energies. Some of the peaks are labeled with the (v, J) quantum numbers of the initial shape resonance state. In each case, these resonances are either the highest or the second-highest quasibound states v for a given J.

state are displayed in Figure 6. The distribution lies in the vicinity of a curve corresponding to equal energy $\epsilon - \omega_P$ in the v, J plane. It spreads from J = 60 down to the lowest J-states. The oscillatory pattern in the distribution along the curve is due Franck−Condon factors. Nevertheless, for the example discussed here, the final population of the (3,58) target state is by far the largest and exceeds that of the second highest, the (19,15) state, by a factor of 56. However, summing up the photoassociation probabilities for all nonresonant J-values yields a non-negligible contribution to the total association probability. Nevertheless, the final population of the (3,58) target state is a factor of 4 larger than the sum of the populations of all other bound states at the end of the laser pulse.

In summary, we find very high state selectivity which originates in the existence of shape resonances. For the shape resonance at ϵ_0 = 3747.4 investigated here, the initial scattering

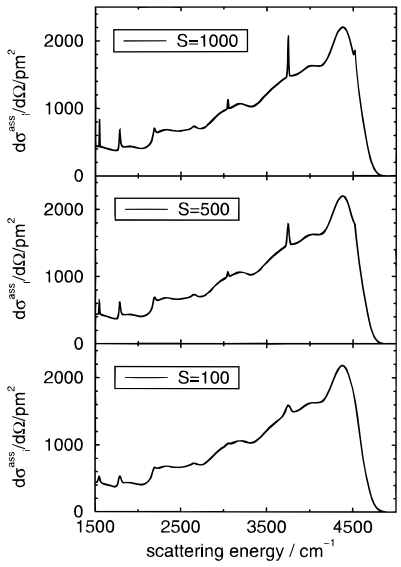

Figure 9. Averaged association cross sections dσ^{ass}/dΩ assuming a nozzle beam velocity distribution for three different values of the speed ratio S vs the mean scattering energy $\hbar^2k_s^2/(2m)$ of the initial state distribution. The resonance peaks correspond to those shown in Figure 7.

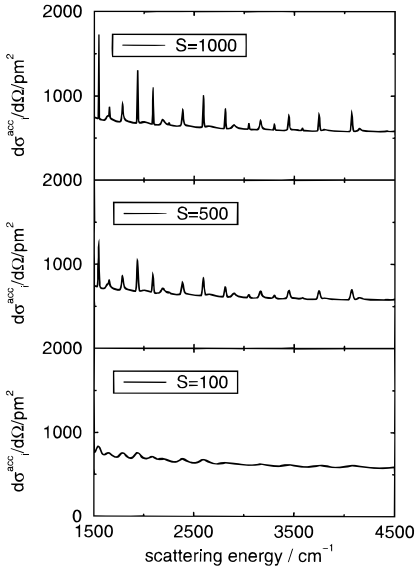

Figure 10. Averaged acceleration cross sections dσ^{acc}/dΩ assuming a nozzle beam velocity distribution for three different values of the speed ratio S vs the mean scattering energy $\hbar^2k_s^2/(2m)$ of the initial state distribution. The resonance peaks correspond to those shown in Figure 8.

state (eq 15) shows a shape resonance only for one specific J-value ($J = 59$). Because of the large overlap of resonance states with the dipole moment function, this partial wave is strongly favored in both the association and acceleration process. The combination with an optimized laser pulse designed to maximize the population of a bound target state results in the observed high state-selectivity.

3.5. Photoassociation Cross Section. In this section, we calculate the association cross section defined in section 2.3 as a function of the scattering energy ϵ. We follow the perturbative treatment of section 2.5 and we use the laser pulse of section 3.2 ($\epsilon_p = 514$ MV/m, $2T_p = 200$ fs, $\omega_p = 4605.9$ cm^{-1}) optimized for the (3,58) ← (7,59) transition. The scattering wave function of eq 15 is used as an initial state. In our calculations, the value of ϵ is varied from 1000 to 5000 cm^{-1} with a step size of $\Delta\epsilon = 1.0$ cm^{-1}. This increment is needed to resolve at least the energetically wider resonances with a lifetime shorter than 5 ps. Our choice of the step size is just small enough to resolve the (7,59) resonance which has an energetic width of slightly more than 1 cm^{-1}. This consideration gives another justification for the choice of this particular shape resonance. Apart from being the energetically most isolated one, its width in energy and time is very favorable. On the one hand, the relatively large energy width can be resolved without resorting to an extremely small energetic step size; on the other hand, the lifetime of about 5.13 ps is long enough to use sub-picosecond laser pulses ($T_p = 100$ fs) to manipulate the resonance state within its lifetime.

Our association spectrum can be seen in Figure 7. First of all, the curve shows a couple of very sharp peaks corresponding to certain bound ← resonance transitions. The largest of these peaks have been identified and labeled by the respective initial and final states in the figure. Although the scattering energy covers almost the whole range of shape resonance states of the HCl molecule, only a small selection of the 176 resonances causes a peak in the spectrum. The reason for this is obvious. According to eq 2, the photon energy ω_p must match the energy difference between a quasibound and a bound state within the width of the effective line shape of the laser pulse (eq 29) which is of the order of a few 100 cm^{-1}. Clearly, the peak for the scattering energy coinciding with the (7,59) shape resonance exhibits the largest photoassociation cross section. This peak is almost exclusively due the (3,58) ← (7,59) transition. Again, this confirms the very high state selectivity of the photoassociation process. The height of the other peaks mostly depends on how closely the transition energy resembles the carrier frequency ω_p of the laser pulse.

Finally, we want to discuss the broad background of the spectrum in Figure 7. This contribution to the photoassociation probability is caused by bound ← free transitions where the initial (free) state does not represent a shape resonance state. It slightly rises with the scattering energy and reaches its maximum at a scattering energy of about $\epsilon = 4400$ cm^{-1}, after which it rapidly falls off. To explain this behavior statistically, we calculate the density of bound states with respect to energy. The stars in Figure 6 give this density per energy interval of 0.01 cm^{-1} shifted by the laser energy $\omega_p = 4606$ cm^{-1}. It increases steeply from low values in the region of the lowest bound states up to a maximum just below the dissociation limit beyond which it disappears. Hence, the density of bound states shows the same qualitative behavior as the background of the photoassociation spectrum thus demonstrating the mainly statistical nature of the photoassociation process in the absence of shape resonances. Only the fact that the rise of the background with increasing energy is slightly steeper than the rise of the density of states is due to the course of the respective Franck−Condon factors.

3.6. Photoacceleration Cross Section. In the following, the cross section for the photoacceleration process due to the absorption of a photon is studied. As in the previous section on photoassociation, we use our perturbative treatment, and we vary the initial scattering energy ϵ from 1000 cm^{-1} to 5000 cm^{-1} with a step size of $\Delta\epsilon = 1$ cm^{-1}. In order to make the association and acceleration cross sections comparable, we use the same optimized laser pulse as in the previous section. Methodologically, the main difference to the treatment of photoassociation in section 3.5 is that the final states are not discrete states but form a continuum of free (scattering) states, see eq 20. We approximate this continuum using a discrete

number of continuum wave functions with a density of one function per energy interval of 1 cm^{-1}. Usually, this density is high enough to obtain converged acceleration cross sections, except if the energy of the final state coincides with a shape resonance. With the optimized frequency of the laser pulse being $\omega_p = 4605.9$ cm^{-1}, only the six energetically highest shape resonances are eligible as target states for photoacceleration of collision pairs with an energy of $\epsilon > 1000$ cm^{-1}. However, with the laser pulse optimized for the (3,58) ← (7,59) transition, the photon energy does not match any of the possible resonance ← resonance transition. Below, we will study this specific process for other photon energies on its own.

The resulting acceleration cross section as a function of the scattering energy is shown in Figure 8. The sharp peaks correspond to certain continuum ← resonance transitions. These are inelastic transitions from a quasibound state to a higher free scattering state. For the main peaks, quantum numbers of the initial state have been assigned in Figure 8. In principle, one should expect all 176 shape resonances to show up in the spectrum whenever the initial scattering energy coincides with any of the resonance energies. This is in contrast to the association spectrum where only those shape resonances are visible for which a bound ← resonance transition is in near-resonance with the laser frequency. However, in the simulations of the photoacceleration process, only about 25 peaks are detected for two different reasons. On the one hand, using a finite step size $\Delta\epsilon = 1$ cm^{-1} (or using a spectroscopic apparatus with this resolution), shape resonances with an energetic width below approximately 0.1 cm^{-1} usually cannot be seen which results in an upper bound for the lifetime of about 50 ps. This excludes relatively low-lying quasibound states. Hence, the main peaks in Figure 8 are caused by the shorter-lived shape resonances. These are typically the highest or second highest of the quasibound states for a given J and are found just below the centrifugal barrier of the effective potential (eq 12). On the other hand, if a shape resonances is extremely close to the centrifugal barrier it has an unusually short lifetime (i.e., in the femtosecond regime). As can be seen for the examples of the (10,53) state at 2896 cm^{-1} or the (12,48) state at 2183 cm^{-1}, these resonances result in a broad and low peak because of their exceeding energetic width of $\Gamma > 30$ cm^{-1}.

As has been discussed for the association spectrum, also the acceleration spectrum exhibits a background caused by free ← free transitions where neither the initial nor the final energy matches any of the shape resonances. This background signal falls off slowly with the scattering energy as a result of the dependence of the Franck−Condon factors for free ← free transitions on the energy of the initial (free) state.

In Figures 2b,c we compare the cross sections of the competing processes in the vicinity of the (7,59) resonance energy. Here we used a smaller step size of $\Delta\epsilon = 0.1$ cm^{-1} to obtain a higher resolution. The peaks of both the photoassociation and photoacceleration cross sections coincide with the jump of the partial scattering phase $\delta_{59}(\epsilon_0)$ (see Figure 2a) again showing the uniqueness of the shape resonance state. For a scattering energy of about $\epsilon = \epsilon_0 = 3747.4$ cm^{-1}, which matches the (7,59) shape resonance, the cross section for photoassociation is about three times larger than that for photoacceleration.

Finally, we also study resonance ← resonance transitions between shape resonance states. As an example, we optimize the laser frequency ω_p with respect to the transition (7,60) ← (7,59). The energy of the (7,60) target state is $\epsilon = 4144$ cm^{-1}. The optimized laser energy is $\omega_p = 423$ cm^{-1} in the far infrared region, which implies a detuning of $\Omega^- = 30$ cm^{-1}. Qualitatively, the cross section behaves like that in Figure 2c. However, the absolute values are considerably larger than for photoassociation or for photoacceleration with the final state being a free state. For the example studied here, the value of the cross section reaches about $\sigma_i^{acc} = 1.45$ nm^2. This value can be compared with e.g. $\sigma_i^{ass} = 0.007$ nm^2 for the optimized (3,58) ← (7,59) transition. Clearly, the huge cross sections for resonance ← resonance transition are due to the very large Franck−Condon factor for a transition with $\Delta v = 0$.

3.7. Averaging. In the previous sections, we always assumed initial scattering states of the form (eq 15) with a sharp momentum $\hbar k$ parallel to $\vec{e}_z$. In the following we want to investigate spectra for a realistic atomic beam scattering experiment. In crossed beam experiments using well collimated beams, the distribution of collision angles can be made sufficiently narrow so that we do not have to consider it here. However, there is a nonnegligible distribution of relative velocities of the collision partners. In order to simulate this spread of velocities, we perform an incoherent average by integrating the association and acceleration cross section over different initial k -values.

$$\bar{\sigma}^{ass/acc} = \int dk\, g(k)\, \sigma_{i=k}^{ass/acc} \tag{36}$$

where $g(k)$ is the distribution function of (relative) velocities. In our investigation we assume the use of supersonic nozzle beams with their typically very narrow velocity distributions

$$g(k) \propto k^2 \exp\left(-\frac{S^2(k-k_s)^2}{k_s^2}\right) \tag{37}$$

Here $\hbar k_s/m$ gives the stream velocity of the beam and S is the speed ratio (stream velocity divided by thermal velocity relative to the former) characterizing the quality of the beam.[28,42]

Figures 9 and 10 show averaged cross sections for photoassociation and photoacceleration of the H + Cl collision pairs, respectively. The results are for a mean scattering energy $\hbar^2 k_s^2/(2m)$ between 1500 and 4500 cm^{-1} and for three different S-values ($S = 100$, 500, 1000). The general trend illustrated in the figures is always such that for decreasing S the peaks associated with the shape resonances are becoming less pronounced with respect to the background which is due to the association/acceleration of free states.

The averaged photoassociation cross sections of Figure 9 show that also after applying the averaging procedure (eq 36) all the peaks in the photoassociation spectrum are still visible. Furthermore, the peak for the (3,58) ← (7,59) transition is somewhat larger than the peaks for any of the other bound ← resonance transitions. However, already for $S = 1000$ its absolute height does not exceed that of the background at around 4400 cm^{-1}. Another interesting aspect is the relative amplitude of the peaks. For example, the narrow, high peak ($i = 13$, 44) and the wide, low peak ($i = 13$, 45) of Figure 7 become comparable upon averaging. This tendency continues for decreasing the speed ratio S. Finally, for $S = 100$ most peaks have disappeared and the remaining (13,44), (13,45), and (7,59) are of comparable size and shape.

Similar trends can be found in the averaged photoacceleration spectra of Figure 10. For $S = 1000$ all the peaks can still be distinguished. However, their height relative to the background has decreased. Also some relative intensities have changed e.g., the two peaks (12,47) and (11,49) around 2000 cm^{-1}). The tendency of broadening increases for $S = 500$. Finally, for S

$= 100$ the shape resonances can only be recognized as small oscillations of the background.

4. Conclusions

We have shown that shape resonances play an important role for the processes of photoassociation and photoacceleration which were investigated previously only using a rotationless model.[16,19] The localization of probability density mainly at internuclear separations shorter than that of the centrifugal barrier where it strongly overlaps with the molecular dipole moment function results in large Franck−Condon factors for transitions from quasibound states to either bound or free states. Thus, shape resonances open an effective way for the manipulation of collision pairs in the electronic ground state by infrared (IR) light. This is in analogy with recent findings on the role of shape resonances in three-body collisions such as collision induced stabilization and dissociation.[27] On the one hand, stimulated emission can lead to photoassociation which may be used to prepare molecules, in particular in extremely high rovibrational states. Thus, photoassociation spectroscopy provides a tool to probe molecular states which are difficult or even impossible to probe by traditional means.[6] On the other hand, the competing absorption of light causes photoacceleration which can be used to prepare collision pairs at higher energies.

The influence of shape resonances together with the use of sub-picosecond laser pulses can be used to control the efficiency and the state selectivity of the photoassociation and photoacceleration process. Because the resonance condition is met only for one specific partial wave occurring in the decomposition of a plane wave describing the initial scattering state, this partial wave is favored in both the association and acceleration process giving rise to high rotational state selectivity. Furthermore, for photoassociation it has been shown that optimization of the laser pulse can also be used to either favor the P or the R branch transition. In addition, vibrational state selectivity of the association product[16] or energy selectivity of an accelerated collision pair[19] can be achieved by optimization of the laser pulse.

In principle, similar results could also be obtained by means of continuous light sources. However, the use of pulsed lasers offers additional advantages: A fascinating possibility could be the observation of buildup or decay of shape resonances in real time by appropriate pump-probe techniques, see ref 9. Moreover, for a permanent association to occur, the laser-induced processes have to be faster than possible relaxation mechanisms (e.g., the collision with third particles, or, in the case of a polyatomic product, the intramolecular energy redistribution). Finally, short laser pulses can be used to enhance the efficency of photoassociation and photoacceleration, especially when the pulses are taylored to an incoming wave-packet which is spatially and temporally well localized. In summary, a combination of the use of a scattering energy coinciding with a shape resonance and the use of optimized IR laser pulses allows the production of molecules in a specific rovibrational state or of collision pairs at specific energy and angular momentum.

An experimental observation of the predicted effects crucially depends on the energy resolution. A first experimental observation was reported recently for the association of laser-cooled atoms.[9] In the present work we suggest an alternative realization in a scattering experiment using crossed atomic beams. On the basis of our calculations, we predict that, (for high beam quality ($S \geq 100$), it should be possible to resolve individual shape resonances in both association and acceleration spectra.

In future work, photoassociation spectroscopy could be used to investigate potential energy functions and (transition) dipole moment functions. In particular, the information gained for very high rovibrational states can be used to refine these functions at very large internuclear distances. Another possible application could be to exploit the very high sensitivity of the optimized laser pulse parameters with respect to the dynamics of the collision pair to generate isotope selected photoassociation products (e.g., H^{35} Cl vs H^{37} Cl). We also want to point out the possibility of using shorter laser pulses to generate coherent superpositions of rovibrational states of the molecular product.[14,15] The corresponding wave-packet dynamics could be probed by excitation into a fluorescing or an ionizing state which would provide a means to image the photoassociation process in real time. Finally, it is a challenge to extend the present approach to other systems including polyatomic hydrides where selective photoassociation or acceleration has to compete with dissipative channels such as intramolecular rovibrational redistribution.

Acknowledgment. Financial support by the *Deutsche Forschungsgemeinschaft* (DFG) through Grant Ma 515/14-2 is gratefully acknowledged. J.M. also thanks the *Fonds der Chemischen Industrie* for continous support. Furthermore, we would like to thank Prof. R. J. LeRoy for a copy of his program LEVEL 6.0.

References and Notes

(1) Dubov, V. S.; Gudzenko, L. I.; Gurvich, L. V.; Iakovlenko, S. I. *Chem. Phys. Lett.* **1977**, *45*, 330.
(2) Frommhold, L. *Collision-Induced Absorption in Gases*; Cambridge University Press: Cambridge, 1993.
(3) Thorsheim, H. R.; Weiner, J.; Julienne, P. S. *Phys. Rev. Lett.* **1987**, *58*, 2420.
(4) Machholm, M.; Giusti-Suzor, A.; Mies, F. H. *Phys. Rev. A* **1994**, *50*, 5025.
(5) Lett, P. D.; Helmerson, K.; Phillips, W. D.; Ratliff, L. P.; Rolston, S. L.; Wagshul, M. E. *Phys. Rev. Lett.* **1993**, *71*, 2200.
(6) Lett, P. D.; Julienne, P. S.; Phillips, W. D. *Annu. Rev. Phys. Chem.* **1995**, *46*, 423.
(7) Suominen, K. A. *J. Phys. B: At. Mol. Opt. Phys.* **1996**, *29*, 5981.
(8) Bohn, J. L.; Julienne, P. S. *Phys. Rev. A* **1996**, *54*, 4637.
(9) Boesten, H. M. J. M.; Tsai, C. C.; Verhaar, B. J.; Heinzen, D. J. *Phys. Rev. Lett.* **1996**, *77*, 5194.
(10) Schloss, J. H.; Jones, R. B.; Eden, J. G. *J. Chem. Phys.* **1993**, *99*, 6483.
(11) Gordon, E. B.; Egorov, V. G.; Nalivaiko, S. E.; Pavlenko, V. S.; Rzhevsky, O. S. *Chem. Phys. Lett.* **1995**, *242*, 75.
(12) Rodriguez, G.; Eden, J. G. *J. Chem. Phys.* **1991**, *95*, 5539.
(13) Marvet, U.; Dantus, M. *Chem. Phys. Lett.* **1995**, *245*, 393.
(14) Gross, P.; Dantus, M. *J. Chem. Phys.* **1997**, *106*, 8013.
(15) Backhaus, P.; Schmidt, B. *Chem. Phys.* **1997**, *217*, 131.
(16) Korolkov, M. V.; Manz, J.; Paramonov, G. K.; Schmidt, B. *Chem. Phys. Lett.* **1996**, *260*, 604.
(17) Korolkov, M. V.; Paramonov, G. K.; Schmidt, B. *J. Chem. Phys.* **1996**, *105*, 1862.
(18) Chelkowski, S.; Bandrauk, A. D. *J. Chem. Phys.* **1993**, *99*, 4279.
(19) Korolkov, M. V.; Schmidt, B. *Chem. Phys. Lett.* **1997**, *272*, 96.
(20) Joseph, T.; Manz, J. *Mol. Phys.* **1986**, *58*, 1149.
(21) Ford, K. W.; Hill, D. L.; Wakano, M.; Wheeler, J. A. *Ann. Phys.* **1959**, *7*, 239.
(22) Child, M. *Molecular Collision Theory*; Academic: London, 1974.
(23) Toennies, J. P.; Weltz, W.; Wolf, G. *J. Chem. Phys.* **1979**, *71*, 614.
(24) Bunker, D. L. *J. Chem. Phys.* **1960**, *32*, 1001.
(25) Roberts, R. E.; Bernstein, R. B.; Curtiss, C. F. *J. Chem. Phys.* **1969**, *50*, 5163.
(26) Whitlock, P. A.; Muckerman, J. T.; Roberts, R. E. *J. Chem. Phys.* **1974**, 60, 3658.
(27) Pack, R. T.; Walker, R. B.; Kendrick, B. K. *Chem. Phys. Lett.* **1997**, *276*, 255.
(28) Scoles, G., Ed. *Atomic and Molecular Beam Methods*; Oxford University Press: New York, 1988.
(29) Adams, G. F.; Chabalowski, C. F. *J. Phys. Chem.* **1994**, *98*, 5878.
(30) Loudon, R. *The Quantum Theory of Light*; Clarendon: Oxford, 1973.

(31) Ogilvie, J. F.; Rodwell, W. R.; Tipping, R. *J. Chem. Phys.* **1980**, *73*, 5221.
(32) Marston, C. C.; Balint-Kurti, G. G. *J. Chem. Phys.* **1989**, *91*, 3571.
(33) Press, W. H.; Teukolsky, S. A.; Vetterling, W. T.; Flannery, B. P. *Numerical Recipes in Fortran*; Cambridge University Press: Cambridge, 1992.
(34) Cohen-Tannoudji, C.; Liu, B.; Laloe, F. *Quantum Mechanics*; Wiley: New York, 1977.
(35) Mahapatra, S.; Sathyamurthy, N. *J. Chem. Phys.* **1997**, *105*, 10934.
(36) Arfken, G. *Mathematical Methods for Physicists*; Academic: Boston, 1985.
(37) Kosloff, R. *Annu. Rev. Phys. Chem.* **1994**, *45*, 145.
(38) Feit, M. D.; Fleck, J. A., Jr.; Steiger, A. *J. Comput. Phys.* **1982**, *47*, 412.
(39) Leforestier, C.; Bisseling, R. H.; Cerjan, C.; Feit, M. D.; Friesner, R.; Guldberg, A.; Hammerich, A.; Jolicard, G.; Karrlein, W.; Meyer, H.-D.; Lipkin, N.; Roncero, O.; Kosloff, R. *J. Comput. Phys.* **1991**, *94*, 59.
(40) Tellinghuisen, J. *Adv. Chem. Phys.* **1985**, *60*, 399.
(41) LeRoy, R. J. *University of Waterloo Chemical Physics Research Report CP-555*; University of Waterloo: Waterloo, Ontario, Canada, 1995.
(42) Levine, R. D.; Bernstein, R. B. *Molecular Reaction Dynamics and Chemical Reactivity*; Oxford University Press: Oxford, 1987.